Nanoscale

PAPER

View Article Online
View Journal | View Issue

Cite this: *Nanoscale*, 2026, **18**, 2625

Esterification synthesis of iron oxide nanoparticle tracers for magnetic particle imaging (MPI)

Ambar C. Velazquez-Albino, [a] Bianca Elsea,[a] Andrii Melnyk,[a] Neel Eswaran,[b] Eric D. Imhoff,[a] Aleia G. Williams,[c] Willem Graham,[c] Jacqueline Anne Johnson, [c] Charles E. Johnson,[c] Megan M. Butala [b] and Carlos M. Rinaldi-Ramos *[a,d]

The potential for producing iron oxide magnetic particle imaging (MPI) tracers using an alternative synthesis method based on esterification of iron oleate with oleyl alcohol was evaluated. The defined reaction mechanism allows monitoring of reaction progress with Fourier Transform Infrared (FTIR) spectroscopy. The influence of reaction temperature and precursor flow rate on esterification reactions of Fe(II) oleate for tuning iron oxide nanoparticle size and dispersity was studied, identifying conditions for producing larger nanoparticles suitable as MPI tracers. Increasing temperature and decreasing flow rates were found to increase the resulting nanoparticle size and reduce dispersity. Furthermore, the effect of the iron source used to prepare the iron oleate precursor was evaluated by characterization of nanoparticle magnetic properties, composition, and MPI performance. Although the nature of the precursor did not appear to affect nanoparticle morphology or growth, it influenced magnetic properties and MPI performance. Saturation magnetization was close to the bulk value of magnetite and the discrepancy between physical and magnetic diameters was lowest for nanoparticles synthesized with oleates prepared using Fe(II) or Fe(III), as opposed to nanoparticles synthesized using an oleate prepared with a 1 : 2 molar mixture of Fe(II) and Fe(III). X-ray diffraction characterized that nanoparticles synthesized using the Fe(III) oleate are the most crystalline, followed by Fe(II) and the 1 : 2 Mix, respectively. Mössbauer spectroscopy was used to verify iron oxide phases, suggesting nanoparticles synthesized using the Fe(III) oleate consist of a mixture of γ-Fe_2O_3 and Fe_3O_4, in contrast to those obtained from the Fe(II) and 1 : 2 Mix oleates, which consisted of a mixture of wüstite, γ-Fe_2O_3 and Fe_3O_4. Characterization of MPI performance using a MOMENTUM™ scanner demonstrated the capability of the esterification reaction to yield high-quality monodisperse MPI tracers.

Received 26th July 2025,
Accepted 13th December 2025

DOI: 10.1039/d5nr03157e

rsc.li/nanoscale

Iron oxide is ubiquitous in nature, but fine control at the nanoscale is crucial for maximizing its potential for many biomedical applications, including magnetic particle imaging (MPI). MPI is a rapidly developing imaging modality that relies on the nonlinear magnetization of superparamagnetic nanoparticles to generate a signal, which is proportional to the tracer mass.[1] This allows for quantification and visualization of tracer distribution in a volume of interest without significant tissue attenuation or applying ionizing radiation.[1] MPI has been applied in pre-clinical studies and holds promise for clinical applications such as cell tracking, blood pool imaging, drug delivery, and stroke detection.[2–14] Tracers with enhanced sensitivity and resolution are critical for advancing MPI applications,[15] where imaging performance is primarily governed by nanoparticle composition, size, and magnetic properties.[16,17] The composition of most MPI tracers is iron oxide, and it is expected that MPI performance improves with the diameter cubed and linearly with the saturation magnetization.[16,17] However, a recent study shows that reducing the discrepancy between physical and magnetic diameters is also key for enhancing MPI performance.[18] For decades, thermal decomposition synthesis has been the gold standard to obtain magnetic nanoparticles suitable for applications that require fine control over nanoparticle size, shape, and properties, including in producing high-quality MPI tracers.[4,11,13,19–25] However, common challenges include formation of mixed iron oxide phases, use of toxic solvents, surface ligand effects, and high temperatures (300–350 °C) than can decompose solvents and surfactants.[26,27] The for-

[a]*Department of Chemical Engineering, University of Florida, Gainesville, FL 32611, USA. E-mail: carlos.rinaldi@ufl.edu*
[b]*Department of Materials Science and Engineering, University of Florida, Gainesville, FL 32611, USA*
[c]*Department of Mechanical, Aerospace and Biomedical Engineering, University of Tennessee Space Institute, Tullahoma, TN 37388, USA*
[d]*J. Crayton Pruitt Department of Biomedical Engineering, University of Florida, Gainesville, FL 32611, USA*

mation of wüstite, an antiferromagnetic iron oxide phase, requires synthesis modifications for oxidation to improve magnetic properties,[28,29] which include post-synthesis oxidation,[18,28] *in situ* synthesis oxidation,[4,29] and addition of oxidizing reagents to the reaction medium, such as dibenzyl ether.[30] Additionally, thermal decomposition has reproducibility challenges and a poorly defined reaction mechanism, which can often hinder optimization.[18,28,31] New synthesis methods that provide fine control of both physical and magnetic properties are attractive for producing new MPI tracers, as further optimization of current methods has proved to be challenging.

The esterification reaction of carboxylic acids with alcohols to produce organic esters at temperatures below 200 °C is widely practiced, and esters compose some of the highest volume of industrial organic compounds produced.[32] More recently, conversion of metal carboxylates to metal hydroxides through esterification in neat alcohol was demonstrated to produce another desirable product – metal oxide nanoparticles.[33] A slow precursor injection technique was implemented to enable production of metal oxide nanoparticles with controlled size.[33,34] This approach is similar to a semi-batch thermal decomposition synthesis,[35] reported to afford better control of nanoparticle properties, albeit at lower temperatures such that thermal decomposition of the precursors should be negligible. Prior work with the esterification synthesis has focused on indium oxide (In_2O_3), with some reports of other metal oxides (*e.g.*, γ-Fe_2O_3, Mn_3O_4, CoO, ZnO) at temperatures below 290 °C, all resulting in oleic acid-stabilized nanoparticles.[34,36–44] For the synthesis of iron oxide nanoparticles, the reaction mechanism involves esterification of iron oleate and oleyl alcohol, catalyzed by the metal ion, producing the ester oleyl oleate and metal hydroxides (Scheme 1). The hydroxyl groups then undergo a dehydration reaction, producing water as a side-product and forming metal oxygen bonds (Fe–O–Fe) that initiate nanoparticle formation. Finally, the remaining oleate ligands on the nanoparticle surface also undergo esterification reactions with oleyl alcohol to further grow the nanoparticle. Removing the water produced is crucial, as it can accelerate metal carboxylate hydrolysis, causing uncontrolled growth and precipitation.[34] Also, because esterification reactions are equilibrium-limited, removal of water and excess of alcohol is desirable in driving the esterification reaction forward.[32] An advantage of this synthesis method is the well-defined reaction mechanism that incorporates oxygen, potentially eliminating the need for oxidation treatments needed with the thermal decomposition synthesis. Additionally, the reaction progress can be monitored *via* Fourier transform infrared (FTIR) spectroscopy. Authors have called this a "living nanoparticle synthesis", similar to polymerization reactions, as it can be stopped and restarted by controlling the precursor addition.[36,45] This continuous synthesis method also provides fast nanoparticle formation, within 60 seconds of precursor addition at 230 °C.[34]

Studies of the synthesis of In_2O_3 have demonstrated that nanoparticle size and uniformity can be increased through tailored reaction conditions, such as increasing reaction temperature from 230 °C to 290 °C and lowering precursor flow rate.[40] Others have shown that surface reactivity of nanoparticles is influenced by the choice of surface capping agent, which in turn affects nanoparticle formation and growth. For example, for In_2O_3 at 290 °C, switching oleyl alcohol to oleylamine results in faster amidation reactions, which results in rapid generation of reactive metal precursors and larger nanoparticles.[44] The esterification synthesis method also yields precise control for doped In_2O_3 nanoparticles, which is challenging in thermal decomposition due to differences in decomposition temperatures and reactivities of different metal precursors.[36,37] Thus far, only a few studies have focused on synthesis of iron oxide.[38,39,41,42] Importantly, intrinsic magnetic properties of iron oxide nanoparticles produced *via* esterification reactions remain largely unreported, as is their characterization for specific applications, including MPI.

The nature of the iron oleate precursor used has been shown to affect nanoparticle properties in both the thermal decomposition[28,35,46–48] and esterification[41] synthesis literature. This is not surprising, as early studies in thermal decomposition used iron pentacarbonate[49,50] or iron acetylacetonate[51,52] salts directly in a batch reactor, but preparing iron oleate precursor as an intermediate has provided finer control.[26,35,53] The influence of iron oleate structure, binding mode, oleic acid content, and purification treatments have

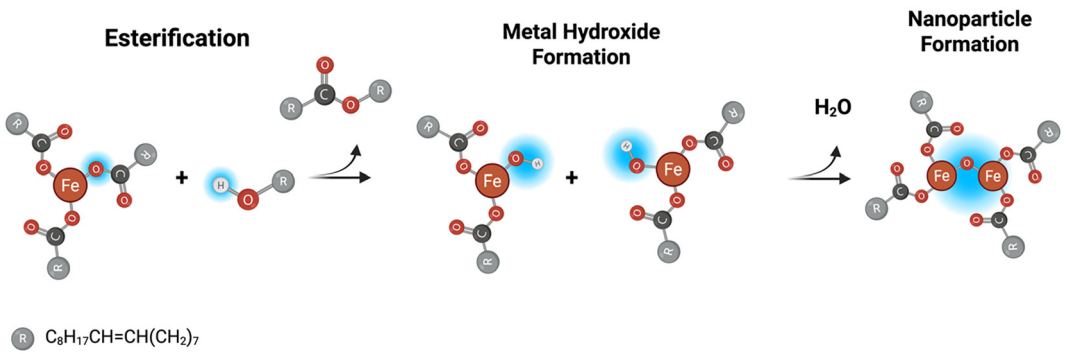

Scheme 1 Reaction mechanism for esterification synthesis of iron oxide nanoparticles.

been shown to affect resulting nanoparticle properties.[28,46] Hence, a method was developed for a reproducible synthesis of iron oleate from Fe(III) acetylacetonate at 325 °C with precise iron concentration that can be used without further purification steps.[35] This oleate has been used to produce magnetite MPI tracers *via* thermal decomposition with oxidation treatments,[4,18,29] motivating comparison to the standard iron oleate precursor primarily used in the esterification synthesis literature, prepared from Fe(II) acetate at 150 °C.[34,38,39,41,42] The effect of iron precursor ligation and oxidation state on iron oxide nanoparticle synthesis *via* the esterification route has been explored at low temperatures of nanoparticle synthesis (230 °C) and precursor synthesis (150 °C).[41] Fe(II) acetate has been the primary salt used for preparing the iron oleate precursor for the esterification synthesis, and nanoparticles produced using an Fe(III) acetylacetonate had twin defects.[41] Although a higher temperature for Fe(III) precursor synthesis (190 °C) led to fewer twin defects, this route was not persued due to the likeliness of reducing the iron, a possibility previously demonstrated by Kemp *et al.*[28] Plummer *et al.* state that after ~3 mmol of Fe addition with the Fe(II) oleate, nanocrystals became highly polydisperse and irreproducible.[41] Therefore, to achieve larger sizes, an Fe(II) and Fe(III) precursor was obtained by mixing the two precursors at a 1 : 2 molar ratio, corresponding to the stoichiometric Fe ratio in magnetite. Addition of 20 mmol of Fe from the mixed oleate at 230 °C resulted in 19 nm nanoparticles, but extending size beyond that faced issues of dispersion after purification.[41]

Here we report a series of studies using the esterification synthesis route to synthesize iron oxide nanoparticles with sizes and magnetic properties suitable for use as tracers in MPI. The effects of higher reaction temperatures (290 °C to 350 °C) and lower precursor flow rates (0.025 mmol min^{-1} to 2.5 mmol min^{-1}) were evaluated to identify conditions resulting in iron oxide nanoparticles of ~20 nm diameter. Nanoparticles obtained under similar synthesis conditions using Fe(II) and Fe(III) oleates, as well as another prepared by a 1 : 2 mixture of them, were characterized physically, magnetically and in terms of their MPI performance.

Results and discussion

Low temperature (290 °C) esterification of Fe(II) oleate yielded iron oxide nanoparticles that were too small to be effective MPI tracers

The esterification synthesis of metal oxide nanoparticles has been reported for a range of temperatures (230–290 °C) and precursor flow rates (0.17–0.35 mL min^{-1}). Although the influence of these parameters has only been studied for indium oxide nanoparticles,[40] these studies suggest that higher temperatures and lower flow rates yield larger and more uniform particles. As such, we initially evaluated the esterification synthesis of iron oxide at a temperature of 290 °C and flow rate of 0.2 mL min^{-1}, as these were at the high range of temperature and low range of flow rate evaluated for indium oxide nanoparticles.[40]

Fourier transform infrared spectroscopy (FTIR) of reaction aliquots (Fig. 1A) facilitates tracking of the reaction progress (Fig. 1B), revealing a halt in the production of esters and the consumption of the iron oleate precursor at around 60 min, which corresponds to the addition of 6 $mmol_{Fe}$. After the growth region denoted in Fig. 1B (i), ester peaks decrease in region (ii) most likely due to decomposition, as the decomposition temperature of the ester oleyl oleate is 250–300 °C.[54] Additionally, in region (ii) the Fe-oleate COO peak starts to increase suggesting it is accumulating in the reactor. This is to be expected if alcohol has been depleted, halting the esterification reactions. The resulting nanoparticles were characterized physically *via* transmission electron microscopy (TEM) to obtain the size distributions shown in Fig. 1C, showing that nanoparticle formation occurs early in the reaction, with a median diameter of 6 nm after 5 minutes, in contrast to thermal decomposition that may require a longer period before nanoparticles are observed.[35,55,56] After 60 min of reaction (6 $mmol_{Fe}$), corresponding to the maximum for the ester peak observed in the FTIR (Fig. 1A and B), the nanoparticles reach a median diameter of 8.6 nm (Fig. 1C). Further addition to 12 $mmol_{Fe}$ produced polydisperse nanoparticles of ~10 nm (Fig. 1C and Fig. S1). Under similar conditions, Plummer *et al.* reported that particles become highly polydisperse after addition of 3 $mmol_{Fe}$.[41] We observe polydisperse nanoparticles from the first aliquot at 5 min, which corresponds to addition of 0.5 $mmol_{Fe}$. Further, the 10 nm particle size obtained is not suitable to be a high-quality single core MPI tracer.[17]

Tuning esterification of Fe(II) oleate reaction temperature and precursor flow rate yields iron oxide nanoparticles with diameters suitable for use as MPI tracers

Temperature and precursor flow rate have been shown to significantly affect indium oxide nanoparticle growth, influencing their size, shape, and quality.[40] Along with the desire to further increase nanoparticle size, this motivated a study to explore the effect of temperature and flow rate for the synthesis of iron oxide nanoparticles with addition of 1 $mmol_{Fe}$. The esterification reaction has been primarily conducted at temperatures between 230–290 °C to mitigate any reducing effects that can occur at higher temperatures and avoid thermal decomposition.[34,41] However, higher temperatures are typically used for the thermal decomposition of iron oleate,[4,18,26,28,29,35,46,53,57] motivating us to study higher temperatures in the esterification synthesis. Increasing temperature from 290 °C to 350 °C resulted in an increase in iron oxide nanoparticle diameter from 6 to 9 nm and a decrease in the geometric deviation ($\ln \sigma_p$) after adding 1 $mmol_{Fe}$ (Fig. 2A and Fig. S2). These results agree with trends reported in a study of indium oxide esterification synthesis, where larger nanoparticles with narrower size distributions were observed at 290 °C, compared to lower temperatures.[40]

Since larger nanoparticles were observed at 350 °C, longer reactions were evaluated at this temperature. A lower flow rate

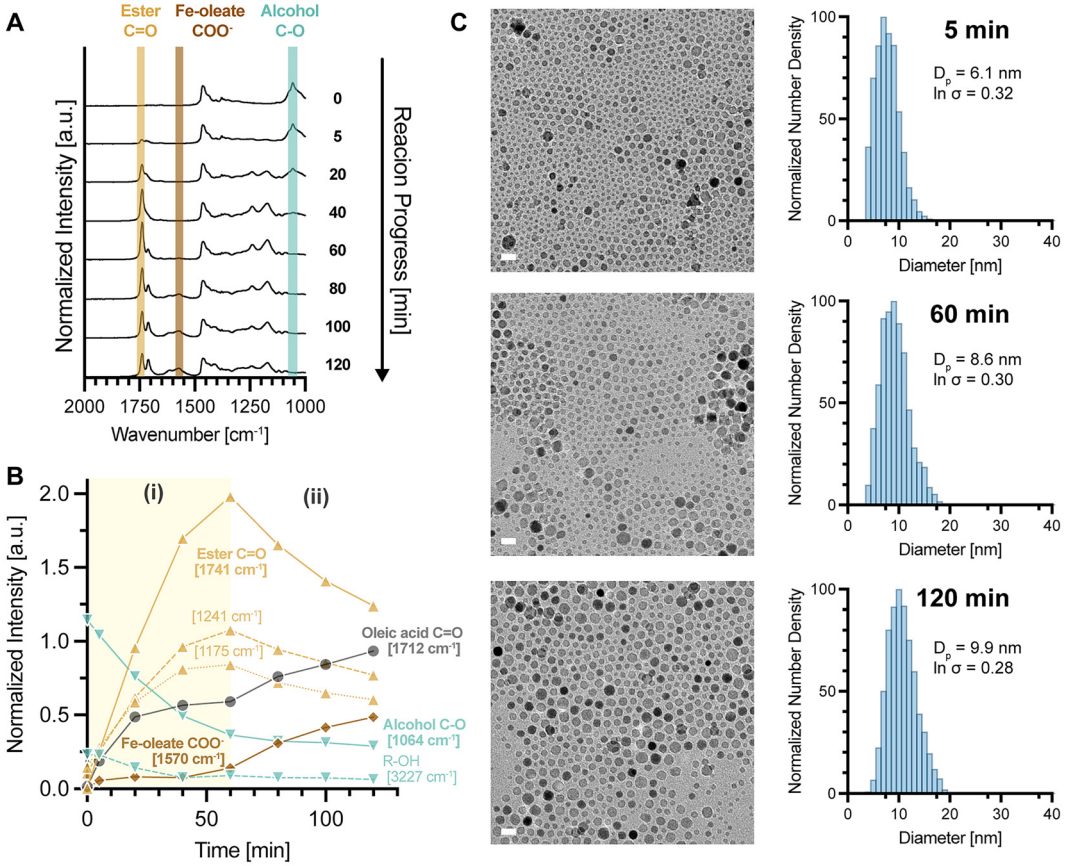

Fig. 1 Low temperature esterification of Fe(II) oleate for synthesis of iron oxide nanoparticles at 290 °C and a precursor addition rate of 0.1 mmol min^{-1} yields particles that are too small to be effective MPI tracers. (A) Fourier Transform Infrared (FTIR) facilitates tracking of reaction progress, as the main peaks for the reagents (iron oleate and oleyl alcohol) and the ester product can be obtained from reaction aliquots. (B) Tracking FTIR intensity over reaction time demonstrates ester formation (yellow) and alcohol consumption (teal) in region (i) with the addition of 6 mmol of Fe. Further addition, results in iron oleate (brown) accumulation due to the alcohol depletion observed in region (ii). (C) Physical size distributions obtained from analysis of transmission electron microscopy (TEM) images show that polydisperse particles of ~6 nm quickly form after 5 min of reaction and grow to a size of ~10 nm after 120 min and 12 mmol Fe is added. Scale bars are 20 nm.

of 0.05 $mmol_{Fe}$ min^{-1} was chosen based on studies with indium oxide.[40] However, attempts to carry out longer reactions at 350 °C proved to be difficult, as FTIR tracking shows depletion of alcohol after 25 min of reaction (Fig. S3A). This is much faster than the 60 min observed for the synthesis at 290 °C (Fig. 1). Still, larger (~13 nm) and more uniform size ($\ln \sigma_p$ = 0.1) nanoparticles were obtained using significantly less iron (Fig. S3B). Precursor addition was halted after 25 min (1.25 $mmol_{Fe}$) and alcohol was replenished by adding 13 mL of oleyl alcohol at 0.35 mL min^{-1}, which was the original volume in the reactor. Yet, this was only partially effective, as FTIR (Fig. S3A) shows a low amount of alcohol in the reactor at the end of alcohol addition (ii), possibly because of boil-off or decomposition. Nevertheless, the particle size analysis (Fig. S3B) demonstrates that nanoparticle size and distribution remain consistent, showing nanoparticle growth stopped once precursor addition was halted. Adding a condenser to reduce oleyl alcohol boil-off resulted in water condensation, leading to a less uniform final nanoparticle product (Fig. S3B). These studies at 350 °C suggested that although increasing temperature yields larger nanoparticles with narrower size distributions, further growth is limited due to depletion of oleyl alcohol, which has a boiling point of 333 °C and starts decomposing at lower temperatures.[54] Based on these observations, subsequent studies were performed at a synthesis temperature of 320 °C.

Next, the influence of iron oleate precursor addition rate was evaluated at 320 °C (Fig. 2B) with addition of 1 $mmol_{Fe}$ at various flow rates. The results in Fig. 2B show that decreasing precursor flow rate resulted in an increase in nanoparticle diameter and a reduction in polydispersity (geometric deviation, $\ln \sigma_p$). However, nanoparticle size increased only to a certain extent, as decreasing the flow rate further from 0.1 $mmol_{Fe}$ min^{-1} resulted in a reduction in nanoparticle size. Representative TEM images are shown in Fig. S4 and results for the effect of flow rate at 350 °C exhibiting the same behavior are shown in Fig. S5. These studies suggest that esterification synthesis of iron oxide nanoparticles at 320 °C and a precursor flow rate of 0.1 $mmol_{Fe}$ min^{-1} may be suitable to produce larger nanoparticles with narrow size distribution.

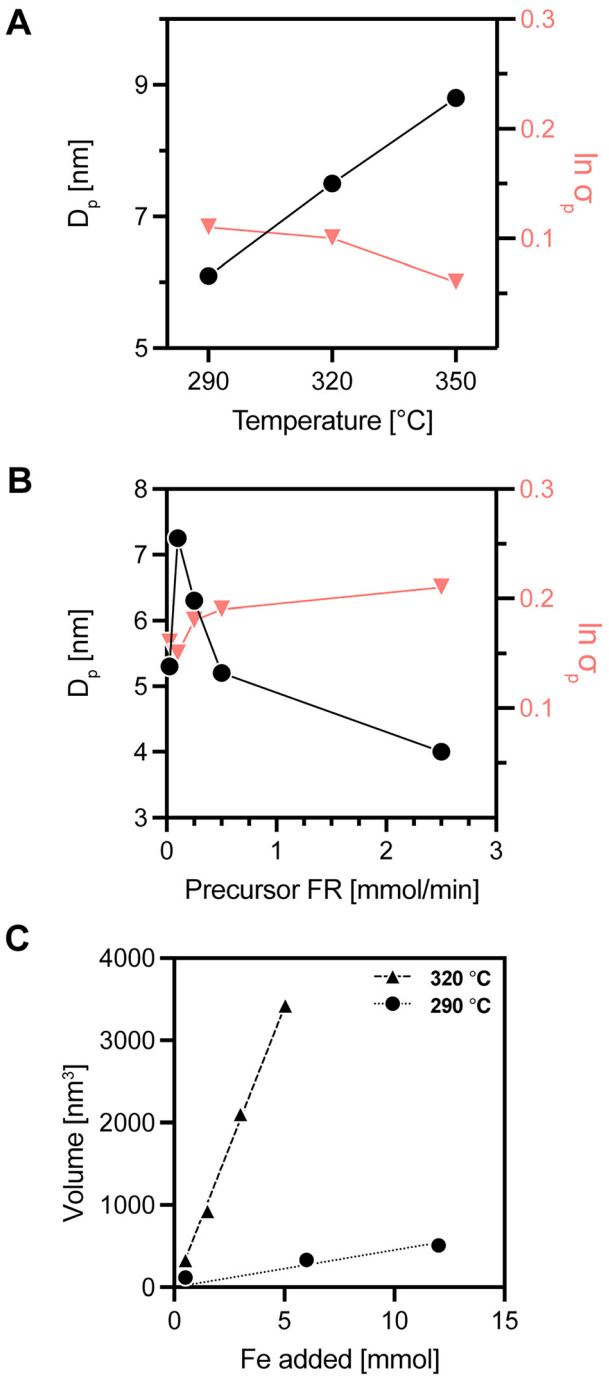

Fig. 2 Higher esterification reaction temperatures and slower precursor addition rates yield larger and more monodisperse nanoparticles. Shorter reactions with addition of 1 mmol of Fe were used to explore the influence of temperature and precursor flow rate for iron oxide nanoparticles. (A) Increasing temperature from 290 °C to 350 °C increases physical diameter (D_p) from 6 to 9 nm and decreases polydispersity (geometric deviation, ln σ_p) after addition of 1 $mmol_{Fe}$ at a rate of 0.175 $mmol_{Fe}$ min^{-1}. (B) Decreasing precursor flow rate to 0.1 $mmol_{Fe}$ min^{-1} increases physical diameter and decreases polydispersity after addition of 1 mmol of Fe at 320 °C. (C) A longer reaction with addition of 5 mmol of Fe at 320 °C and 0.1 $mmol_{Fe}$ min^{-1} shows a significant increase in nanoparticle growth rate compared to the original conditions explored in Fig. 1 (290 °C and 0.1 $mmol_{Fe}$ min^{-1}).

Finally, we evaluated nanoparticle growth for longer esterification syntheses at 290 °C and 320 °C, and a precursor flow rate of 0.1 $mmol_{Fe}$ min^{-1} (Fig. 2C). Both synthesis temperatures preserve the expected linear growth in nanoparticle volume with $mmol_{Fe}$ added to the reaction, suggesting that these grow continuously, with a larger rate of growth for nanoparticles synthesized at 320 °C. These results agree with studies of In_2O_3 nanoparticle synthesis, where growth rate increased with increasing reaction temperature from 230 °C to 290 °C.[40] The synthesis at 320 °C yielded particles of ~18 nm with addition of 5 $mmol_{Fe}$ at 0.1 $mmol_{Fe}$ min^{-1}, suggesting this condition is appropriate to obtain nanoparticles that are suitable for MPI. This motivated subsequent studies using these conditions to explore other synthesis parameters.

The nature of the iron oleate precursor did not influence nanoparticle morphology or growth trends

Next, we evaluated the effect of iron oleate precursor composition, as it has been demonstrated to influence nanoparticle properties in both thermal decomposition and esterification synthesis.[28,35,46,48] Fe(II) and Fe(III) oleates were prepared *via* methods corresponding to those commonly used in esterification and thermal decomposition syntheses using $Fe(ac)_2$ and $Fe(acac)_3$, respectively. The oxidation state of iron in the salts used to prepare the iron oleates was used to label the corresponding oleates and differentiate the nanoparticles obtained using them in this study. Additionally, a mixed oleate was produced at a 1 : 2 molar ratio of Fe(II) : Fe(III), which is labeled as the 1 : 2 Mix oleate. FTIR spectra of Fe(II) and Fe(III) oleates are shown in Fig. S6, highlighting the main peaks of interest to compare them. The carboxylic acid C=O stretch of oleic acid at 1710 cm^{-1} was used to calculate the percentage of free oleic acid in the oleate by comparing to the absorbance of pure oleic acid. The Fe(II) oleate contains 62% free oleic acid and the Fe(III) oleate contains 35% free oleic acid. The metal carboxylate IR bands were observed in the range of 1650–1510 cm^{-1} for the asymmetrical vibrations, and 1500–1375 cm^{-1} for the symmetric vibrations.[46] The separation ($\Delta\nu$) of the bands in these regions has been used to deduce the carboxylate coordination mode. The maximum peak absorbance in these regions were subtracted to obtain a $\Delta\nu$ of 184 cm^{-1} and 159 cm^{-1} for the Fe(II) and the Fe(III) oleates, respectively, which corresponds to a bridging coordination mode. These results suggest that the Fe(II) and Fe(III) oleates contain similar metal carboxylate coordination modes but have a notable difference in their free oleic acid content. The latter is to be expected as the oleic acid to metal ratio is 6.3 and 5 for the Fe(II) and Fe(III) oleate synthesis procedures, respectively, and the stoichiometric amount required for Fe(II) and Fe(III) salts is different as well.

The same volume of Fe(II) and Fe(III) precursors (8 mL) was added to each reactor at 320 °C to test the influence of iron oleate precursor on nanoparticle properties. Due to their different iron concentrations (0.5 M for the Fe(II) oleate, 0.63 M for the Fe(III) oleate, and 0.58 M for the 1 : 2 Mix oleate), the number of moles of Fe used in the reaction varied from 4 to

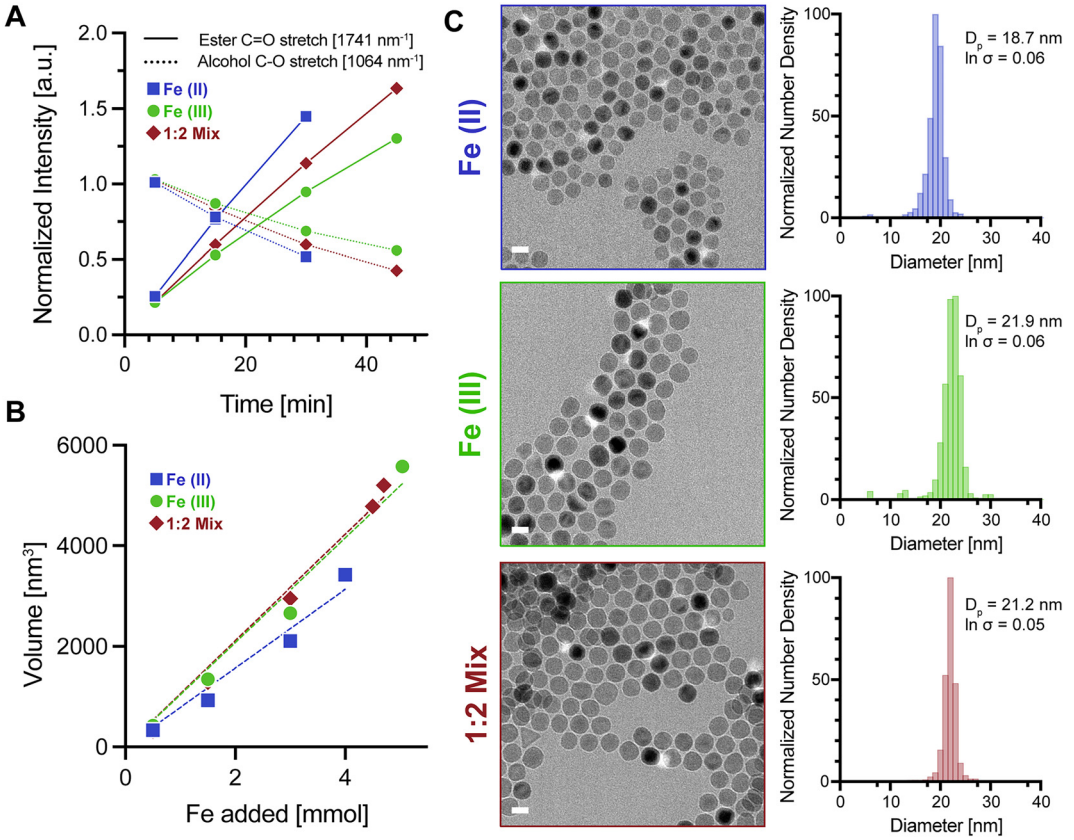

Fig. 3 Esterification synthesis of iron oxide nanoparticles using iron oleates prepared from different iron salts resulted in similar nanoparticle growth trends and morphologies. (A) FTIR tracking of the main ester and alcohol peaks show similar behavior for reactions using the Fe(II), Fe(III), and 1 : 2 Mix oleates. (B) Similar trends in nanoparticle growth were observed for reactions with all three oleates. (C) TEM images and corresponding physical diameter distribution histograms show similar size, shape, and distribution of nanoparticles for reactions with all three oleates. Scale bars are 20 nm.

5 $mmol_{Fe}$. Comparing trends in FTIR peaks associated with ester formation and oleyl alcohol consumption (Fig. 3A) suggests similar rates of ester formation and alcohol consumption for the three oleates. Furthermore, similar nanoparticle growth trends were observed for the three oleates (Fig. 3B). Finally, similar nanoparticle morphology and size distributions were observed for the final product of each synthesis (Fig. 3C and Fig. S6). Although the median physical diameter for the nanoparticles obtained using the Fe(II) oleate was smaller (18.7 nm) than that obtained with the Fe(III) and 1 : 2 Mix oleate (21.9 nm and 21.2 nm), it must be noted that there is a 1 $mmol_{Fe}$ difference in the iron added to that reaction compared to the Fe(III) oleate. These observations suggest that esterification synthesis at 320 °C and 0.1 $mmol_{Fe}$ min^{-1} using these three oleates results in similar nanoparticle morphologies, growth trends, and size distributions.

The nature of the iron oleate precursor influences the magnetic properties and composition of iron oxide nanoparticles obtained *via* esterification synthesis

Nanoparticle composition and magnetic properties influence MPI performance,[17] hence further characterization of nanoparticles obtained *via* esterification synthesis using the three oleates is crucial. The basic adiabatic theory of x-space MPI suggests that signal strength and resolution both improve with increasing initial magnetic susceptibility and saturation magnetization of the nanoparticle tracer.[16,17] According to the Langevin model for superparamagnetism, the initial susceptibility increases with the cube of the nanoparticle diameter. Additionally, prior work highlights the importance of minimizing discrepancy between physical and magnetic diameters for improving MPI performance.[18]

Magnetic properties were evaluated by measuring magnetization of nD-PEG coated nanoparticles in water as a function of applied magnetic field at 300 K (Fig. 4A and Fig. S7). All three nanoparticles display superparamagnetic behavior, with no observed hysteresis and with magnetic saturation. The initial susceptibility was largest for nanoparticles synthesized using the Fe(III) oleate, followed by nanoparticles synthesized using the Fe(II) oleate, and then nanoparticles synthesized using the 1 : 2 Mix oleate. Magnetic diameters (D_m) were estimated by fitting the magnetization measurements to the Langevin function, weighted by a lognormal diameter distribution. Results in Table 1 show that nanoparticles synthesized

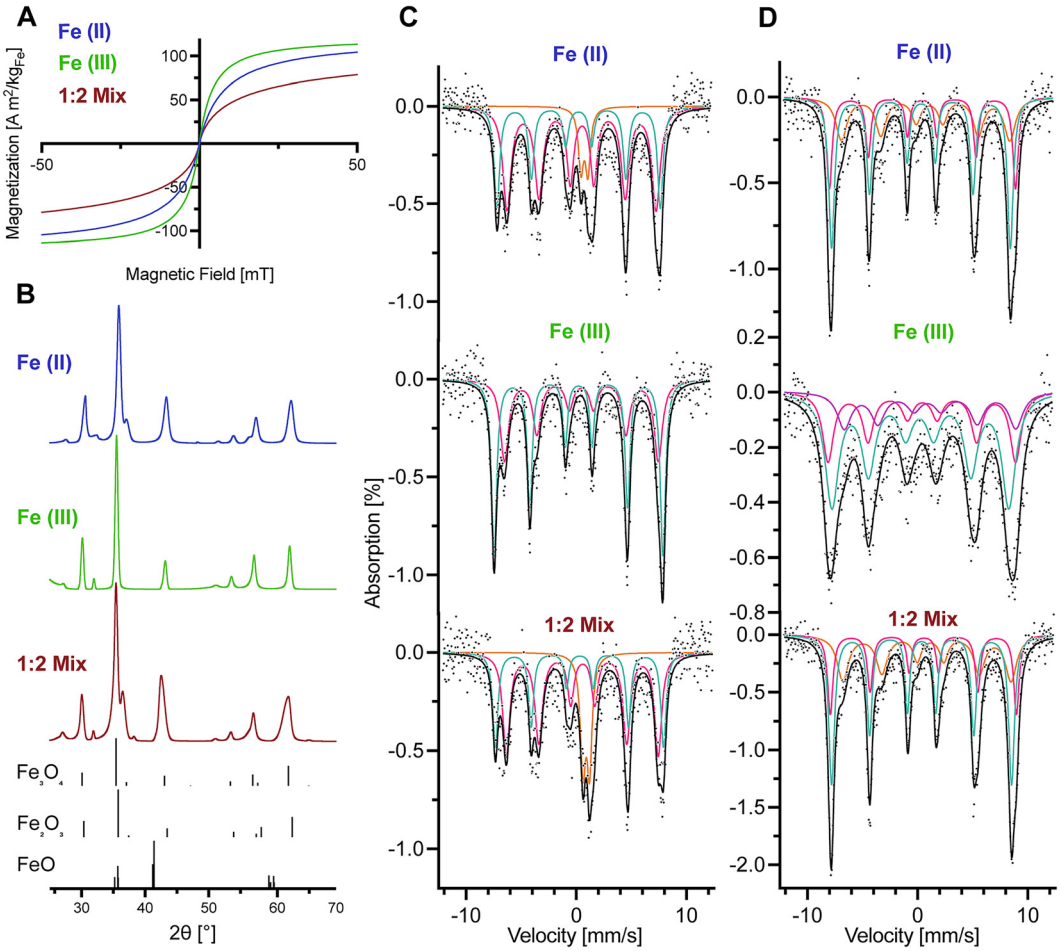

Fig. 4 Different mixtures of iron oxide phases are observed for esterification synthesis using various iron oleate precursors (Fe(II), Fe(III), and 1 : 2 Mix). (A) Magnetization *vs.* magnetic field curves at 300 K of nD-PEG coated nanoparticles used to estimate magnetic diameters (D_m) and saturation magnetizations (M_s). (B) X-ray diffraction (XRD) at 1.5 A shows broad magnetite (Fe_3O_4) or maghemite (γ-Fe_2O_3) peaks for Fe(II) and 1 : 2 Mix samples, as these are indistinguishable with XRD, meanwhile, sharper peaks were obtained for the Fe(III) sample. (C) Mössbauer spectroscopy at 293 K, with fitted subspectra corresponding to magnetite A (tetrahedral) site Fe^{3+} and maghemite A & B sites Fe^{3+} (teal sextet), magnetite B (octahedral) site $Fe^{2.5+}$ (valence averaged, pink sextet), and Wüstite ($Fe_{1-x}O$) Fe^{2+} site (orange doublet). (D) Mössbauer spectroscopy at 6 K, with fitted subspectra corresponding to magnetite A (tetrahedral) site Fe^{3+} and maghemite A & B sites Fe^{3+} (teal sextet), magnetite B (octahedral) site Fe^{3+} (pink sextet), magnetite B-site Fe^{2+} and wüstite ($Fe_{1-x}O$) Fe^{2+} site (orange sextet), and magnetite B-site Fe^{2+} (purple sextet).

using the Fe(III) oleate possess the largest magnetic diameter, 20 nm, compared to those synthesized using the Fe(II) and 1 : 2 Mix oleates, with 16 nm and 12.5 nm, respectively. The saturation specific magnetizations for all three nanoparticles are shown in Table 1 and are close to the value for bulk magnetite (120 A m^2 kg_{Fe}^{-1}). The nanoparticles obtained using the Fe(III) oleate had the smallest discrepancy between physical and magnetic diameters (1.9 nm), and a high saturation magnetization (128 A m^2 kg_{Fe}^{-1}). Next, the nanoparticles obtained with the Fe (II) oleate had similarly high saturation magnetization (127 A m^2 kg_{Fe}^{-1}), but a larger discrepancy between physical and magnetic diameters (2.7 nm). Finally, the nanoparticles synthesized using the 1 : 2 Mix oleate had a high (but comparably lower) saturation magnetization (115 A m^2 kg_{Fe}^{-1}), and the largest discrepancy between physical and magnetic diameters (8.7 nm). This discrepancy between physical and magnetic diameters was observed in 20 nm commercial nanoparticles from Ocean Nanotech and has been studied in the thermal decomposition synthesis, where an oxidizing agent is needed to reduce the so-called "magnetic dead layer".[29] Sub-10 nm iron oxide particles prepared from the Fe(II) oleate *via* the esterification synthesis at lower temperature (230 °C) were previously shown to have very similar physical and magnetic diameters,[39] but a larger discrepancy is observed for the larger nanoparticles obtained at the reaction conditions of this study.

Iron oxide phases were identified using X-ray diffraction (XRD), which show broader peaks for nanoparticles synthesized using the Fe(II) and 1 : 2 Mix oleates, relative to the sharper peaks for nanoparticles synthesized using the Fe(III) oleate (Fig. 4B). This difference in broadening is most clearly observed in peaks at higher angles (50–65°). The locations and

Table 1 Properties obtained from characterization of iron oxide nanoparticles synthesized at 320 °C using different iron oleate precursors at an addition flow rate of 0.1 mmol min^{-1}

Properties	Fe(II)	Fe(III)	1 : 2 Mix
D_p [nm]	18.7	21.9	21.2
$\ln \sigma_p$	0.06	0.06	0.05
D_m [nm]	16	20	12.5
$\ln \sigma_m$	0.33	0.26	0.57
$D_p - D_m$	2.7	1.9	8.7
Crystal size – D_{XRD} [nm]	13.1	17.1	14.8
Crystal size error [nm]	0.8	0.8	0.9
$D_p - D_{XRD}$	5.6	4.8	6.4
M_s [A m^2 kg_{Fe}^{-1}]	128	127	115
Fe_3O_4 (Fe%)[a]	87%	63%	78%
γ-Fe_2O_3 (Fe%)[a]	4%	37%	5%
FeO (Fe%)[a]	9%	0%	17%
MPI signal intensity [a.u. per mg Fe]	77.4	108.5	40.7
MPI FWHM [mT]	10.5	8.6	10.4

[a] Based on site relative areas obtained from fitting of 293 K Mössbauer spectra.

relative intensities of the most prominent peaks were consistent with magnetite (Fe_3O_4) and maghemite (Fe_2O_3) crystal structures. However, these two phases are difficult to distinguish due to their similar XRD patterns and, further, the broadening that results from the nanometer-scale sizes. Despite their similarities and peak broadening, there was evidence of coexistence of the magnetite and maghemite phases in the Fe(II) and 1 : 2 Mix samples. The shoulder in the 35° peak and the shift in the 44° peak indicate a mixed phase product, but no peaks indicate the formation of the wüstite (FeO) phase. The absence of FeO is an advantage to thermal decomposition methods, where the formation of this nonmagnetic phase has been demonstrated before being oxidized to Fe_3O_4 or Fe_2O_3.[46,58–60] However, detection of small impurities or other iron oxide phases can be difficult due to overlapping peaks, along with peak broadening. Minos peaks observed at 27, 32, and 51° suggest iron oxide hydroxide species, but cannot be fully resolved and identified at the measurement conditions. Previous XPS characterization reported the presence of surface hydroxyls on the nanoparticle along with oleate ligands at lower synthesis temperatures.[34] These observations can motivate further characterization of the nanoparticle surface to investigate the potential of forming iron oxide hydroxides with long-range ordering detectable by XRD. Crystallite sizes estimated using Scherrer's equation and the main peaks are shown in Table 1 and were largest for the nanoparticles obtained using the Fe(III) oleate (17.1 nm), followed by those synthesized using the 1 : 2 Mix oleate (14.8 nm), and those synthesized using the Fe(II) oleate (13.1 nm). Crystal sizes determined from XRD have been previously found to correlate with the magnetic diameters estimated from analysis of the equilibrium magnetization curves, as the magnetic dipole is a result of the crystal's long-range ferroic ordering.[29] This motivated comparison in this study, where the crystallite sizes (D_{XRD}) did not match the magnetic sizes (D_m). However, the discrepancy between physical and magnetic diameters ($D_p - D_m$) correlates with the discrepancy between physical and crystal sizes ($D_p - D_{XRD}$) (Table 1), which suggests one can be informative of the other.

Further characterization using ^{57}Fe Mössbauer spectroscopy probes the environment of iron atoms, providing information on oxidation states and phase compositions. Stacked Mössbauer spectra of samples measured at 293 K are displayed in Fig. 4C, with hyperfine fit parameters in Table S1. All samples exhibit two magnetically split spinel sextets: a tetrahedral A-site Fe^{3+} component (teal) and an octahedral B-site valence-averaged ($Fe^{2.5+}$) component characteristic of magnetite above the Verwey transition (pink). In addition, the nanoparticles obtained using the Fe(II) and 1 : 2 Mix oleates show a central Fe^{2+} doublet (orange) attributed to wüstite (FeO), whereas the Fe(III) oleate sample does not. Stacked spectra at 6 K are displayed in Fig. 4D, with fit parameters in Table S2. At low temperature, all samples display three spinel sextets: tetrahedral A site Fe^{3+} (teal), octahedral B site Fe^{3+} (pink), and a distinct octahedral B site Fe^{2+} sextet (purple) that is indicative of magnetite. Additionally, sextets assigned to wüstite Fe^{2+} (orange) were observed for the Fe(II) and 1 : 2 Mix oleate samples. Fe-atom fractions corresponding to magnetite, maghemite, and wüstite (Table 1) were from the 293 K site areas. The wüstite fraction was taken from its doublet area (Site 3 in Table S1) and excluded from the spinel total. The maghemite fraction was calculated by subtracting half of the area assigned to the $Fe^{2.5+}$ valence averaged site (Site 2 in Table S1) from the area assigned to Magnetite A (tetrahedral) site Fe^{3+} and Maghemite A & B sites Fe^{3+} (Site 1 in Table S2). Estimated maghemite contents for each sample are indicated in Table 1. These estimates indicate that nanoparticles synthesized using the Fe(III) oleate correspond to a mixture of magnetite and maghemite, whereas the nanoparticles synthesized using the Fe(II) and 1 : 2 Mix oleates contain wüstite and a mixture of magnetite and maghemite, with a spinel fraction dominated by maghemite.

The oxidation state of the Fe oleate precursors prepared in this study were not investigated, but oxidative decarboxylation of the oleate has been reported to reduce Fe(III) to Fe(II) starting at temperatures below 180 °C.[28] Although the oleate precursor is dripped into the reactor for the esterification synthesis, the Fe(III) oleate synthesis method used requires heating it over 300 °C, which could cause reduction to Fe(II). This mechanism could explain formation of Fe_3O_4 from the Fe(III) oleate precursor, but further investigation would be necessary.

Prior studies have demonstrated partial oxidation of magnetite nanoparticles when bubbling with air or O_2, with the extent of oxidation being dependent on the ligand at the particle surface and being minimal for oleic acid coated particles and maximal for particles coated with tetramethylammonium hydroxide.[61] During our ligand exchange at 101 °C the particles are suspended in toluene, there is no bubbled oxygen source, and are coated initially with oleic acid and eventually with the much stronger capping agent nitroDOPA-PEG. Because of this combination of low oxygen solubility in toluene, no active source of oxygen, and particles coated with

strong ligands we do not expect significant oxidation during the ligand exchange process and leave study of this potential phenomenon to future work.

Regardless, the Fe(III) oleate tailored for thermal decomposition yields highly crystalline magnetic nanoparticles obtained by esterification synthesis at high temperature. Optimizing both reaction conditions and iron sources eliminated the need to synthesize both Fe(II) and Fe(III) precursors to yield larger Fe_3O_4 nanoparticles. Although particle growth and morphology were similar using the three oleates, they differed in their magnetic properties, crystallinity, and Mössbauer spectra. The high saturation magnetization and crystallinity, along with the small discrepancy between physical and magnetic diameters, suggests the nanoparticles synthesized from the Fe(II) and Fe(III) oleates have potential as high sensitivity and resolution MPI tracers.

Esterification synthesis yields MPI tracers with high sensitivity and resolution performance

First, we evaluated the point spread function (PSF) for each nanoparticle, using the RELAX™ module in the MOMENTUM™ MPI scanner (Fig. 5A). In the PSF, signal intensity corresponds to sensitivity and the full width half-maximum (FWHM) corresponds to resolution. Nanoparticles

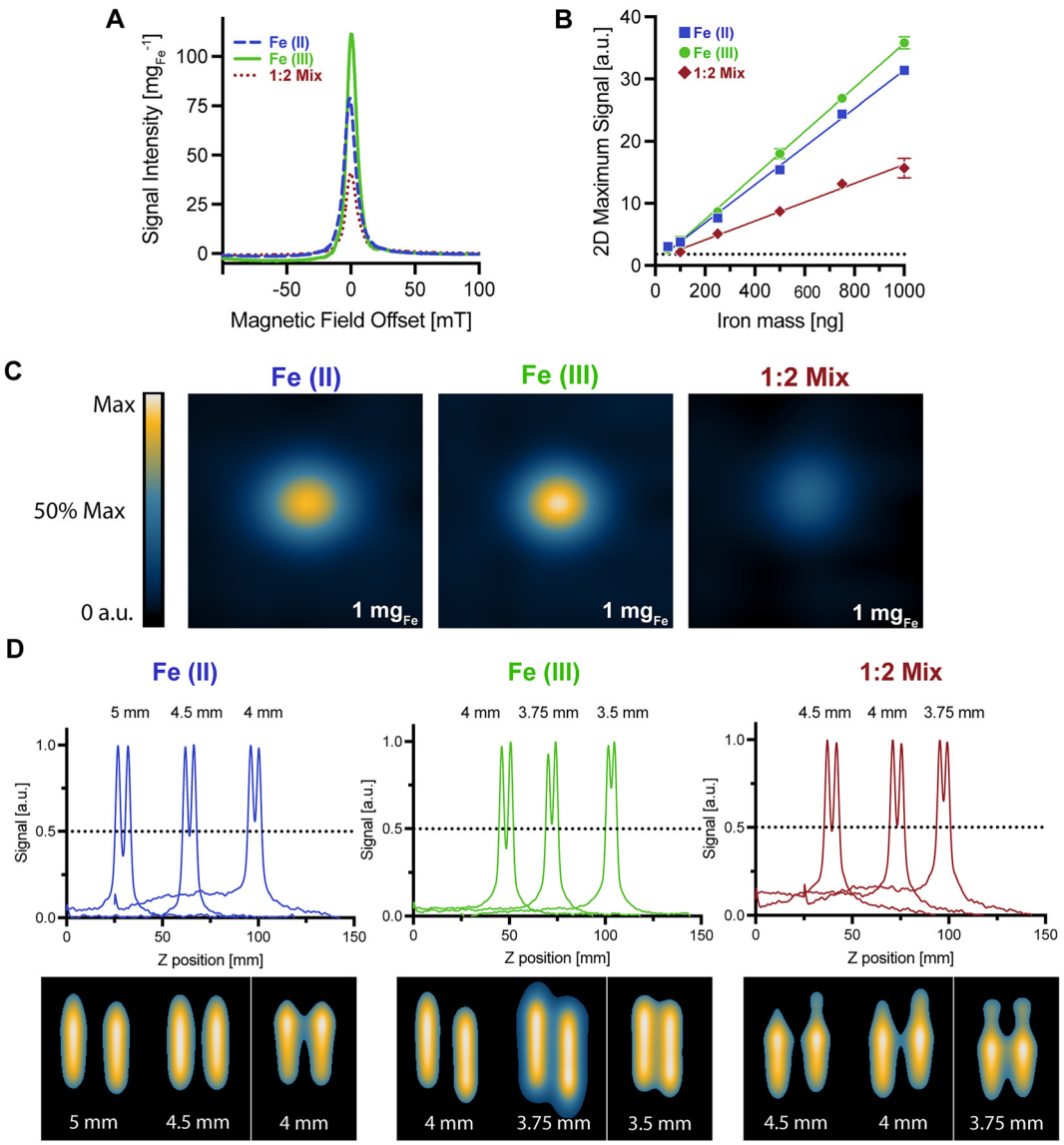

Fig. 5 Esterification synthesis yields high-quality iron oxide MPI tracers with various precursors at optimized reaction conditions. (A) Comparison of signal intensity and resolution (FWHM) based on RELAX™ scans show superior performance for nanoparticles synthesized with Fe(III) oleate. (B) 2D MPI scans of serial dilutions in standard mode show the expected linear relationship between signal and iron mass for all samples, agreeing with the higher signal obtained from RELAX™ scans for the Fe(III) sample. (C) 2D scans of 1 mg of Fe for the three tracers are shown for visual comparison. (D) Line scans of linear resolution phantoms agree with expectations from RELAX™ scans, showing signals of Fe(III) sample can be separated by smaller distances than the Fe(II) and 1 : 2 Mix samples.

synthesized using the Fe(II) and Fe(III) oleates had a high signal intensity, with values of 77.4 and 108.5 mg_{Fe}^{-1}, respectively. In contrast, nanoparticles synthesized using the 1 : 2 Mix oleate had a lower sensitivity of 40.7 mg_{Fe}^{-1}, which agrees with expectations based on the larger discrepancy between physical and magnetic diameters and poorer crystallinity. The nanoparticles synthesized using the Fe(II) and 1 : 2 Mix oleates had similar FWHM of 10.5 and 10.4 mT, respectively. Nanoparticles synthesized using the Fe(III) oleate had a lower FWHM of 8.6 mT, which suggests superior imaging resolution. The nanoparticles synthesized using the 1 : 2 Mix oleate had similar magnetic properties and MPI performance as VivoTrax in our scanner,[62] meanwhile the nanoparticles synthesized using the Fe(II) and Fe(III) oleates had superior magnetic properties and MPI performance. Specifically, nanoparticles synthesized using the Fe (III) oleate have comparable performance to VivoTrax+, a recently developed version enhancing MPI performance to a signal intensity of 97.5 mg_{Fe}^{-1} and a FWHM of 7.1 mT. These results suggest that the esterification synthesis is a valuable route for synthesizing and optimizing monodisperse MPI tracers.

MPI 2D standard mode scans were obtained for serial dilutions of each of the nanoparticles, resulting in the expected linear relationship between MPI signal and iron mass (Fig. 5B). The dotted horizontal line represents the background signal of non-magnetic material based on the average signal of water samples. For nanoparticles synthesized using the Fe(II) and Fe(III) oleates, a real signal in the known location of the sample was observed down to 50 ng_{Fe}, meanwhile for the nanoparticles synthesized using the 1 : 2 Mix oleate a real signal was distinguished down to 100 ng_{Fe}. Fig. 5C shows 2D scans comparing 1 mg_{Fe}, which shows the nanoparticles synthesized using the Fe(III) oleate had a brighter signal, followed by nanoparticles synthesized using the Fe(II) and 1 : 2 Mix oleates, respectively. To compare resolution, standard 2D imaging was used to obtain line scans of resolution phantoms separated by various distances until the signal between them has a signal higher than half of the maximum signal. This corresponds to separation of signal when the signal between the two sources is less than half the maximum (dotted line in Fig. 5D). This allows for estimating imaging resolution, where results show that the signals from the nanoparticles synthesized using the Fe(III) oleate are well separated at a distance between 3.75–4 mm, meanwhile the nanoparticles synthesized using the Fe(II) and 1 : 2 Mix oleates require distance larger than 4 mm to have well separated signals.

Conclusions

This study demonstrates the use of an esterification synthesis method to obtain high-quality MPI tracers with fine control of nanoparticle size, properties, and composition, highlighting an alternative approach to the often-used thermal decomposition synthesis. The results show that tracking the reaction progress with FTIR can facilitate optimization and tuning of reaction conditions for new applications. Nanoparticle growth curves demonstrate continuous growth, which allows for control of nanoparticle size. Comparison of different iron oleates demonstrated limited effects on nanoparticle physical properties, but more strongly influenced magnetic properties and phase composition. Crystal size estimates and quantification of Fe_3O_4 : γ-Fe_2O_3 ratios with XRD and Mössbauer spectroscopy, respectively, suggest that nanoparticles synthesized using the Fe(III) oleate were the most crystalline and consisted of a mixture of maghemite and magnetite, meanwhile Fe(II) and the 1 : 2 Mix oleate resulted in a mixture of wüstite, magnetite, and maghemite. All samples exhibit decent performance as MPI tracers, with the nanoparticles synthesized with the Fe(III) oleate having the best MPI performance in this study, comparable to that of VivoTrax+. The synthesis of magnetic nanoparticles mediated by esterification reactions in a biocompatible solvent shows tremendous potential for MPI, along with other biomedical applications. The ability to track reaction progress *via* FTIR and the incorporation of oxygen in the reaction mechanism makes this synthesis method attractive for further optimization of size and composition with fine control of nanoparticle properties.

Materials and methods

Materials

Iron(III) acetylacetonate (>98% pure) was purchased from TCI American (Portland, OR). Iron(II) acetate (95%), oleic acid (90% technical grade), and diethyl ether (certified ACS) were purchased from Sigma-Aldrich (St Louis, MO). Oleyl alcohol (80–85% technical grade), hexane (>98.5%, certified ACS), toluene (>99.5%, certified ACS), ethanol (200 proof), and tetrahydrofuran (THF, 99.8% for HPLC) were purchased from Thermo Fisher Scientific (Waltham, MA). Copper transmission electron microscopy (TEM) grids (carbon film only, 200 mesh) were purchased from TED PELLA, Inc. (Redding, CA).

Synthesis of iron(II) oleate precursor

The iron(II) oleate was prepared by mixing 1.39 g of iron(II) acetate (8 mmol) and 16 mL of oleic acid (14.24 g, 45.6 mmol based on 90% purity) in a 100 mL three neck flask. The reactor was then connected to a Schlenk line, placed in a heating mantle, and mixed using a borosilicate magnetic stir bar with a stir plate. The mixture was vacuum purged three times, holding vacuum (~0.2–0.3 Torr) for 5 minutes each time and then purging with argon gas. Then, argon flow rate was set to 50 sccm and the reactor was wrapped with quartz wool insulation before ramping to 150 °C. After reaching the reaction temperature, the reaction was soaked for 1 hour. Finally, the reactor was removed from the heating mantle and allowed to cool before use for nanoparticle synthesis. A drop of the iron oleate was scanned *via* FTIR to determine the percentage of free oleic acid and identify the oleate structure.

Synthesis of iron(III) oleate precursor

The iron(III) oleate was prepared according to published work with some modifications. Iron(III) acetylacetonate (22.38 g, 63.36 mmol) was combined with oleic acid (89.48 g, 316.80 mmol) in a 1 : 5 molar ratio inside a 500 mL 3-neck round-bottom flask. The flask was then introduced into a molten metal bath set at 110 °C, with a condenser, thermocouple, and overhead stirrer in the 3 necks. The condenser was connected to a chiller set to 12 °C and attached to the right neck of the reactor. The overhead stirrer, set up in the middle neck, was set to a rate of 350 rpm. The thermocouple and gas flow needle were held by a septum in the left neck with the argon gas flow set to 100 sccm. Once the equipment was set up, the molten metal bath was ramped up in temperature to a set point of 325 °C at a rate of 6.2 °C min^{-1}. After the reaction crossed 300 °C, close monitoring required taking aliquots with a syringe and stainless-steel needle through the septum in the left neck. FTIR was used to scan aliquots in real time and determine the reaction end point, controlling the percentage of free oleic acid left in the oleate. Once the free oleic acid present in the precursor mixture was estimated to be close to 35%, the reactor was removed from the heater and allowed to cool to room temperature before leaving it under vacuum overnight, prior to iron oxide nanoparticle synthesis the next day.

Synthesis of iron oxide nanoparticles

The setup for the synthesis of iron oxide nanoparticles through esterification reactions is shown in Scheme S1. First, 13 mL of oleyl alcohol (34.98 mmol based on 85% purity) were added to a 100 mL three-neck flask, placed in a heating mantle, and mixed using a borosilicate glass coated magnetic stir bar with a stir plate. The reactor's left neck was connected to the Schlenk line, and the middle neck had a rubber septum with a thermocouple. A glass stopper was added to the right neck of the reactor before starting a vacuum treatment for 1 hour while heating to 140 °C. After the vacuum treatment, the reactor was purged with Argon. The flow rate of Argon through the reactor was set to 100 sccm using a mass flow controller, and the glass stopper in the right neck of the reactor was removed. Then, the reactor was wrapped with quartz wool insulation before heating to the desired reaction temperature (290–350 °C tested in these studies). After reaching the reaction temperature in the reactor, the iron oleate was dripped from the middle neck of the reactor at a controlled flow rate using a syringe pump. The range of 0.05–5 mL min^{-1} (0.025–2.5 mmol min^{-1}) was tested in these studies. For the shorter experiments adding 1 $mmol_{Fe}$ no aliquots were taken, but for longer reactions aliquots were taken every 20 minutes for FTIR and TEM characterization.

Nanoparticle purification

Nanoparticles were purified using hexane and ethanol solvent–antisolvent washes with circular magnetic Halbach arrays to remove reaction byproducts and any remaining reagents. Synthesized nanoparticles were well homogenized after storage, and 1 mL of reaction mixture was added to a 15 mL centrifuge tube. This was followed by the addition of 0.3 mL of hexane, vortexing, and addition of 1 mL of ethanol. This solution was lightly mixed before inserting into a circular Halbach array for 10 minutes. The supernatant was discarded by decanting while keeping the tube in the Halbach array, and nanoparticles were resuspended in 0.75 mL of hexane. After mixing and adding 1 μL of oleic acid to ensure none of the surface oleic acid groups are displaced, cup horn sonication was used for 1 minute at 80% amplitude. Again, 1 mL of ethanol was added to the nanoparticle solution, lightly mixed, and inserted into the Halbach array for 10 minutes. The supernatant was discarded, and the last step repeated two more times. After the final supernatant was discarded, nanoparticles were resuspended in 1 mL toluene. Aliquots were taken to perform iron quantification prior to the ligand exchange process.

Iron quantification UV-Vis absorbance assay

To quantify iron in both the nanoparticle toluene and water purified solutions, a 1,10-phenanthroline colorimetric assay was employed. First, 10 μL of the nanoparticle solution (based on this assay, [Fe] ~ 3–5 and 1–2 mg_{Fe} mL^{-1} for toluene and water solutions, respectively) was digested in 1 mL of 70% HNO_3, prepared in triplicate, and placed in a heating block at 101 °C overnight. An aliquot (10–20 μL) of each digested sample was dried in a separate vial, leaving behind a crust. Then, 46 μL of deionized water and 30 μL of hydroxylamine hydrochloride (8 M) were added and mixed by pipetting into each sample before allowing the reaction to reduce iron for 1 h. To complex with Fe^{2+}, 49 μL of sodium acetate (1.2 M) and 75 μL of 1,10-phenenthraline monohydrate (13 mM) were mixed before aliquoting 100 μL of each final sample solution into a 96-well polystyrene plate for absorbance measurements at 508 nm in a SpectraMax M5 microplate reader. Concentrations for each sample were determined by relating the absorbance to a calibration curve prepared from an iron standard solution.

nD-PEG particle coating

First, 22 mg of nD-PEG (nitroDOPA-Polyethylene Glycol) was dissolved in 4.276 mL of toluene at 101 °C. The solution was homogenized and 0.724 mL of nanoparticles suspended in toluene were added (4 mg mL^{-1} concentration). Calculations were performed for a monolayer of PEG in accordance with previous work, using 5 times excess of nD-PEG.[63–66] The solution was ultrasonicated for 90 seconds to minimize aggregates and then left in a heating block at 101 °C for 24 hours for the ligand exchange. Then, nanoparticles were separated by antisolvent enhanced magnetic separation using diethyl ether at a 1 : 3 ratio and placing the vial in a circular Halbach array for 10 minutes. The supernatant was discarded, and the nanoparticles were resuspended in THF. Diethyl ether was added again at a 1 : 1.5 ratio before placing in the circular Halbach array for 10 minutes. This wash was repeated 4 times to remove excess nD-PEG. After the final wash, nanoparticles

were resuspended in deionized water, passed through a 0.22 μm filter to remove aggregates, and filtered using a Miltenyi Biotech LS magnetic column to further purify and concentrate the nanoparticles. Dynamic Light Scattering (DLS) measurements were used to confirm nanoparticle coating and stability in deionized water.

Nanoparticle characterization

Transmission electron microscopy. Transmission electron microscopy (TEM) was used to acquire information about the size distribution of iron oxide nanoparticles. Oleic acid-stabilized particles suspended in hexane were loaded onto 200-mesh copper grids with carbon film and imaged using a FEI Talos F200i S/TEM. Images were analyzed using a custom TEM Image Analysis Graphical User Interface (GUI) program in MATLAB, which was developed to perform physical analysis of particles in TEM images based on the area segmented. We included at least 1000 particles in the analysis to report physical diameters (D_p), and size distribution statistics. The number median physical diameter (D_{pg}) and geometric deviation ($\ln \sigma_p$) of the particle size distribution were obtained by fitting the size distribution histograms to the log–normal distribution ($n_N(D_p)$):

$$n_N(D_p) = \frac{1}{\sqrt{2\pi} D_p \ln \sigma_p} \exp\left(-\frac{\ln^2 D_p/D_{pgv}}{2 \ln^2 \sigma_g}\right) \quad (1)$$

Magnetometry and magnetic diameter fitting. Magnetic properties were evaluated using a magnetic property measurement system (MPMS-3) superconducting quantum interference device (SQUID) magnetometer from Quantum Design, Inc. (Santa Clara, CA, USA). nD-PEG-coated nanoparticles were loaded in PTFE sample holders, while suspended in 100 μL of deionized water at concentrations from 1–2 mg_{Fe} mL^{-1}. Magnetization *versus* magnetic field (*MH*) curves were acquired at 300 K to confirm superparamagnetic behavior (Fig. S7) and fit the data to the Langevin function for superparamagnetism (eqn (2)–(4)), weighted using a log–normal size distribution ($n_V(D_m)$) (eqn (4)) as suggested by Chantrell *et al.*[67]

$$M(\alpha) = M_s \int_0^\infty n_v(D_m) L(\alpha) dD_m \quad (2)$$

$$L(\alpha) = \coth \alpha - \frac{1}{\alpha}; \quad \alpha = \frac{\pi \mu_0 M_d {D_m}^3 H}{6 k_B T} \quad (3)$$

$$n_v(D_m) = \frac{1}{\sqrt{2\pi} D_m \ln \sigma_m} \exp\left[-\frac{\ln^2 (D_m/D_{mv})}{2 \ln^2 \sigma}\right] \quad (4)$$

where α is the Langevin parameter, M_s is the saturation magnetization, D_{mv} is the volume-weighted median magnetic diameter, $\ln \sigma_m$ is the geometric deviation of the magnetic diameter distribution, μ_0 is the permeability of free space, k_B is Boltzmann's constant, M_d is the domain magnetization, and T is the absolute temperature. The fitting of the magnetization curves to these equations using a nonlinear regression model in MATLAB provided an estimate of the average magnetic diameters, under the assumption that the magnetic domains are spherical. The saturation magnetization (M_s) was obtained from the maximum of the *MH* curve, normalized by mass of iron.

X-ray diffraction. A Rigaku MiniFlex600 X-ray diffractometer (40 kV, 15 mA) equipped with a D/teX Ultra2 detector was used to characterize the crystal structure of iron oxide nanoparticles. For sample preparation, 300 μL of purified nanoparticles in hexane were drop casted into a zero-background holder and scanned from 10 to 70° at a step width of 0.005° and scan speed of 0.10° min^{-1}. The SmartLab Studio II software was used for analysis, starting with peak evaluation, fitting them to the split pseudo-Voigt function, and performing background refinement using the B-spline type. Estimates of crystal size used the Scherrer equation and peak broadening of the main peaks were averaged (30, 35, 53, and 56°).

MPI performance. MPI performance of nD-PEG coated nanoparticles in deionized water was first characterized by acquiring MPI RELAX™ scans (45 kHz, 16 mT in *x*-axis) of 5–15 μL (1–2 mg mL^{-1}) in 200 μL microcentrifuge tubes using the MOMENTUM™ scanner (Magnetic Insight, CA, USA). Each sample was placed in custom 3D-printed sample holder, centered in the MPI field of view (FOV), and scanned for 3–5 min. The signal of the *x*-space point spread function (PSF) obtained was normalized by iron mass for comparison. The MPI signal corresponds to the peak specific intensity reported in unit of mg_{Fe}^{-1}, and the resolution corresponds to the FWHM system-reported value in units of mT.

A dilution series of each of the nanoparticles synthesized using the Fe(II), Fe(III), and 1 : 2 Mix oleates were prepared for iron masses from 1000 ng_{Fe} to 25 ng_{Fe} for a 5 μL sample volume. Triplicates were included for each sample by placing 3 capillary tubes (0.8 mm ID) with 5 μL each perpendicular to the FOV. MPI scans were acquired with the MOMENTUM™ scanner (Magnetic Insight, CA, USA) using standard multichannel mode (45 kHz for *x*/*z* axes, 5.7 T m^{-1}). The images obtained through an *x*-space direct reconstruction, which applies an equalization filter,[68,69] were analyzed using MATLAB (Mathworks, MA, USA) in-house algorithms in which the region of interest (ROI) was selected to obtain the maximum signal of each sample. The limit of detection is based on comparison to the signal obtained for a water sample, indicating the background signal of nonmagnetic material, to make sure that the signal obtained from dilute samples is from the nanoparticles and not background signal fluctuations.

To evaluate imaging resolution of each sample, 2 capillary tubes (0.8 mm ID) with 5 μL (5–10 μg) each were placed parallel to the FOV separated by varying distances from the center of the samples (3.5–5 mm) and scanned with the MOMENTUM™ scanner (Magnetic Insight, CA, USA) in 2D standard mode with an *x*-space direct reconstruction (45 kHz for *x*/*z* axes, 5.7 T m^{-1}). The separation between the samples was decreased until the signal could not be separated, using the criteria that signals are separated when it is less than half the maximum signal in between the two capillaries. Finally, line scan profiles were obtained for the section with the

maximum signal for the image, and these were normalized by the maximum signal to facilitate comparisons.

Mössbauer spectroscopy. Mössbauer spectroscopy measurements were performed with a ^{57}Co source, a Janis SHI-850-5 cryogen-free cryostat, and Lakeshore 325 Temperature Controller. Hyperfine interaction parameters were analyzed using a least-squared fitting model with Mössbauer GenFit Software (R. S. Preston and D. E. Brown). Powdered samples were stored in an Argon atmosphere glovebox and were loaded and sealed into Mössbauer cups for characterization at 293 K and 6 K. Additional analysis details are provided in the SI.

Author contributions

A. C. V. A. and C. M. R. R. conceptualized and designed the experiments. A. C. V. A. and B. E. performed nanoparticle synthesis and purification experiments. E. D. I. performed the Fe (III) oleate synthesis. A. C. V. A. performed TEM, SQUID, and XRD characterization of nanoparticles. N. E. performed polymer synthesis and coating of nanoparticles. A. W. performed Mössbauer spectroscopy experiments under J. A. J. supervision. C. E. J. and W. G. performed fitting and interpretation of Mössbauer spectra. A. M. and A. C. V. A. performed MPI experiments.

A. C. V. A. analyzed FTIR and SQUID data, meanwhile B. E. assisted her with TEM analysis. A. C. V. A. and M. M. B. analyzed XRD data. A. M., A. C. V. A., and C. M. R. R. analyzed MPI data. A. C. V. A. and C. M. R. R. contributed equally to visualization of the data. A. C. V. A. wrote the original draft, with main review and editing from C. M. R. R., and review of all co-authors. The manuscript was written through contributions of all authors. All authors have given approval to the final version of the manuscript.

Conflicts of interest

CRR is an inventor on patents and patent applications, which are awarded or submitted in whole or in part to the University of Florida and are related to magnetic nanoparticles or magnetic particle imaging. The university may benefit financially from their commercialization, and the author could benefit under the university's patent policy. All other authors declare that they have no other competing interests.

Abbreviations

MPI	Magnetic particle imaging
FTIR	Fourier transform infrared
nD-PEG	nitroDOPA-polyethylene glycol
DLS	Dynamic light scattering
THF	Tetrahydrofuran
MPMS-3	Magnetic property measurement system
SQUID	Superconducting quantum interference device
FOV	Field of view
PSF	Point spread function
ROI	Region of interest
D_p	Physical diameter
$\ln \sigma_p$	Geometric deviation of physical diameter
$\Delta\nu$	Separation of FTIR bands
D_m	Magnetic diameter
$\ln \sigma_m$	Geometric deviation of magnetic diameter
XRD	X-ray diffraction
FWHM	Full width half-maximum
2D	Two-dimensional

Data availability

The authors confirm that the data supporting the findings of this study are available within the article and its supplementary information (SI). The raw datasets generated supporting the current study are available from the corresponding author on reasonable request.

Supplementary information: scheme of experimental setup; additional representative TEM images of all samples; results of longer synthesis at 350 °C; results of flow rate experiment at 350 °C; FTIR spectra of Fe(II) and Fe(III) oleates; full *MH* curves; tabulated Mössbauer spectroscopy hyperfine fitting parameters measured at 293 K and 6 K. See DOI: https://doi.org/10.1039/d5nr03157e.

Acknowledgements

This manuscript is the result of funding by the National Institutes of Health (NIH) through the National Institute for Biomedical Imaging and Bioengineering (NIBIB) under award number R01EB031224, the National Cancer Institute (NCI) under award R21CA263653, and the National Institute of Neurological Disorders and Stroke (NINDS) under award R21NS125089. It is subject to the NIH Public Access Policy. Through acceptance of this federal funding, NIH has been given a right to make this manuscript publicly available in PubMed Central upon the Official Date of Publication, as defined by NIH. This work was partly conducted at the Nanoscale Research Facility of the Herbert Wertheim College of Engineering at the University of Florida. Thank you to Dr D. J. Milliron and Ph.D. student A. Singh at the University of Texas at Austin for allowing A. C. Velazquez-Albino to visit their laboratory and learn their methods for the esterification synthesis. We are grateful to D. P. Valdes for reviewing the manuscript.

References

1 B. Gleich and J. Weizenecker, Tomographic imaging using the nonlinear response of magnetic particles, *Nature*, 2005, **435**(7046), 1214–1217.

2 A. Rivera-Rodriguez, L. B. Hoang-Minh, A. Chiu-Lam, N. Sarna, L. Marrero-Morales, D. A. Mitchell and C. M. Rinaldi-Ramos, Tracking adoptive T cell immunotherapy using magnetic particle imaging, *Nanotheranostics*, 2021, **5**(4), 431–444.

3 A. Rivera-Rodriguez and C. M. Rinaldi-Ramos, Emerging Biomedical Applications Based on the Response of Magnetic Nanoparticles to Time-Varying Magnetic Fields, *Annu. Rev. Chem. Biomol. Eng.*, 2021, **12**(1), 163–185.

4 S. Liu, A. Chiu-Lam, A. Rivera-Rodriguez, R. DeGroff, S. Savliwala, N. Sarna and C. M. Rinaldi-Ramos, Long circulating tracer tailored for magnetic particle imaging, *Nanotheranostics*, 2021, **5**(3), 348–361.

5 G. Song, M. Chen, Y. Zhang, L. Cui, H. Qu, X. Zheng, M. Wintermark, Z. Liu and J. Rao, Janus Iron Oxides @ Semiconducting Polymer Nanoparticle Tracer for Cell Tracking by Magnetic Particle Imaging, *Nano Lett.*, 2018, **18**(1), 182–189.

6 Q. Wang, X. Ma, H. Liao, Z. Liang, F. Li, J. Tian and D. Ling, Artificially Engineered Cubic Iron Oxide Nanoparticle as a High-Performance Magnetic Particle Imaging Tracer for Stem Cell Tracking, *ACS Nano*, 2020, **14**(2), 2053–2062.

7 O. C. Sehl and P. J. Foster, The sensitivity of magnetic particle imaging and fluorine-19 magnetic resonance imaging for cell tracking, *Sci. Rep.*, 2021, **11**(1), 22198.

8 J. J. Gevaert, K. Van Beek, O. C. Sehl and P. J. Foster, VivoTrax+ improves the detection of cancer cells with magnetic particle imaging, *Int. J. Mag. Part. Imag.*, 2022, **8**(2), 481.

9 A. Antonelli, P. Szwargulski, E.-S. Scarpa, F. Thieben, G. Cordula, G. Ambrosi, L. Guidi, P. Ludewig, T. Knopp and M. Magnani, Development of long circulating magnetic particle imaging tracers: use of novel magnetic nanoparticles and entrapment into human erythrocytes, *Nanomedicine*, 2020, **15**(8), 739–753.

10 J. Rahmer, A. Antonelli, C. Sfara, B. Tiemann, B. Gleich, M. Magnani, J. Weizenecker and J. Borgert, Nanoparticle encapsulation in red blood cells enables blood-pool magnetic particle imaging hours after injection, *Phys. Med. Biol.*, 2013, **58**(12), 3965–3977.

11 A. P. Khandhar, P. Keselman, S. J. Kemp, R. M. Ferguson, P. W. Goodwill, S. M. Conolly and K. M. Krishnan, Evaluation of PEG-coated iron oxide nanoparticles as blood pool tracers for preclinical magnetic particle imaging, *Nanoscale*, 2017, **9**(3), 1299–1306.

12 H. Kratz, A. Mohtashamdolatshahi, D. Eberbeck, O. Kosch, F. Wiekhorst, M. Taupitz, B. Hamm, N. Stolzenburg and J. Schnorr, Tailored Magnetic Multicore Nanoparticles for Use as Blood Pool MPI Tracers, *Nanomaterials*, 2021, **11**(6), 1532.

13 R. Orendorff, A. J. Peck, B. Zheng, S. N. Shirazi, R. M. Ferguson, A. P. Khandhar, S. J. Kemp, P. Goodwill, K. M. Krishnan, G. A. Brooks, D. Kaufer and S. Conolly, Firstin vivotraumatic brain injury imaging via magnetic particle imaging, *Phys. Med. Biol.*, 2017, **62**(9), 3501–3509.

14 J. W. M. Bulte, P. Walczak, M. Janowski, K. M. Krishnan, H. Arami, A. Halkola, B. Gleich and J. Rahmer, Quantitative "Hot-Spot" Imaging of Transplanted Stem Cells Using Superparamagnetic Tracers and Magnetic Particle Imaging, *Tomography*, 2015, **1**(2), 91–97.

15 L. M. Lechermann, D. Lau, B. Attili, L. Aloj and F. A. Gallagher, In Vivo Cell Tracking Using PET: Opportunities and Challenges for Clinical Translation in Oncology, *Cancers*, 2021, **13**(16), 4042.

16 P. W. Goodwill and S. M. Conolly, The X-Space Formulation of the Magnetic Particle Imaging Process: 1-D Signal, Resolution, Bandwidth, SNR, SAR, and Magnetostimulation, *IEEE Trans. Med. Imaging*, 2010, **29**(11), 1851–1859.

17 A. C. Velazquez-Albino, E. D. Imhoff and C. M. Rinaldi-Ramos, Advances in engineering nanoparticles for magnetic particle imaging (MPI), *Sci. Adv.*, 2025, **11**(2), eado7356.

18 A. C. Velazquez-Albino, A. Nozka, A. Melnyk, H. J. Good and C. M. Rinaldi-Ramos, Post-synthesis Oxidation of Superparamagnetic Iron Oxide Nanoparticles to Enhance Magnetic Particle Imaging Performance, *ACS Appl. Nano Mater.*, 2023, **7**(1), 279–291.

19 M. Graeser, T. Knopp, P. Szwargulski, T. Friedrich, A. von Gladiss, M. Kaul, K. M. Krishnan, H. Ittrich, G. Adam and T. M. Buzug, Towards Picogram Detection of Superparamagnetic Iron-Oxide Particles Using a Gradiometric Receive Coil, *Sci. Rep.*, 2017, **7**(1), 6872.

20 P. Keselman, E. Y. Yu, X. Y. Zhou, P. W. Goodwill, P. Chandrasekharan, R. M. Ferguson, A. P. Khandhar, S. J. Kemp, K. M. Krishnan, B. Zheng and S. M. Conolly, Tracking short-term biodistribution and long-term clearance of SPIO tracers in magnetic particle imaging, *Phys. Med. Biol.*, 2017, **62**(9), 3440–3453.

21 P. Ludewig, N. Gdaniec, J. Sedlacik, N. D. Forkert, P. Szwargulski, M. Graeser, G. Adam, M. G. Kaul, K. M. Krishnan, R. M. Ferguson, A. P. Khandhar, P. Walczak, J. Fiehler, G. Thomalla, C. Gerloff, T. Knopp and T. Magnus, Magnetic Particle Imaging for Real-Time Perfusion Imaging in Acute Stroke, *ACS Nano*, 2017, **11**(10), 10480–10488.

22 M. G. Kaul, T. Mummert, C. Jung, J. Salamon, A. P. Khandhar, R. M. Ferguson, S. J. Kemp, H. Ittrich, K. M. Krishnan, G. Adam and T. Knopp, In vitro and in vivo comparison of a tailored magnetic particle imaging blood pool tracer with Resovist, *Phys. Med. Biol.*, 2017, **62**(9), 3454–3469.

23 E. Y. Yu, P. Chandrasekharan, R. Berzon, Z. W. Tay, X. Y. Zhou, A. P. Khandhar, R. M. Ferguson, S. J. Kemp, B. Zheng, P. W. Goodwill, M. F. Wendland, K. M. Krishnan, S. Behr, J. Carter and S. M. Conolly, Magnetic Particle Imaging for Highly Sensitive, Quantitative, and Safe *in Vivo* Gut Bleed Detection in a Murine Model, *ACS Nano*, 2017, **11**(12), 12067–12076.

24 E. Y. Yu, M. Bishop, B. Zheng, R. M. Ferguson, A. P. Khandhar, S. J. Kemp, K. M. Krishnan, P. W. Goodwill

and S. M. Conolly, Magnetic Particle Imaging: A Novel in Vivo Imaging Platform for Cancer Detection, *Nano Lett.*, 2017, **17**(3), 1648–1654.

25 R. M. Ferguson, A. P. Khandhar, S. J. Kemp, H. Arami, E. U. Saritas, L. R. Croft, J. Konkle, P. W. Goodwill, A. Halkola, J. Rahmer, J. Borgert, S. M. Conolly and K. M. Krishnan, Magnetic Particle Imaging With Tailored Iron Oxide Nanoparticle Tracers, *IEEE Trans. Med. Imaging*, 2015, **34**(5), 1077–1084.

26 J. Park, K. An, Y. Hwang, J.-G. Park, H.-J. Noh, J.-Y. Kim, J.-H. Park, N.-M. Hwang and T. Hyeon, Ultra-large-scale syntheses of monodisperse nanocrystals, *Nat. Mater.*, 2004, **3**(12), 891–895.

27 T. Gevart, B. Freis, T. Vangijzegem, M. L. A. Ramirez, D. Stanicki, S. Begin and S. Laurent, Design of Iron Oxide Nanoparticles as Theranostic Nanoplatforms for Cancer Treatment, in *Topics in Applied Physics*, Springer International Publishing, 2024, pp. 175–215.

28 S. J. Kemp, R. M. Ferguson, A. P. Khandhar and K. M. Krishnan, Monodisperse magnetite nanoparticles with nearly ideal saturation magnetization, *RSC Adv.*, 2016, **6**(81), 77452–77464.

29 M. Unni, A. M. Uhl, S. Savliwala, B. H. Savitzky, R. Dhavalikar, N. Garraud, D. P. Arnold, L. F. Kourkoutis, J. S. Andrew and C. Rinaldi, Thermal Decomposition Synthesis of Iron Oxide Nanoparticles with Diminished Magnetic Dead Layer by Controlled Addition of Oxygen, *ACS Nano*, 2017, **11**(2), 2284–2303.

30 R. Chen, M. G. Christiansen, A. Sourakov, A. Mohr, Y. Matsumoto, S. Okada, A. Jasanoff and P. Anikeeva, High-Performance Ferrite Nanoparticles through Nonaqueous Redox Phase Tuning, *Nano Lett.*, 2016, **16**(2), 1345–1351.

31 L. M. Liz-Marzán, C. R. Kagan and J. E. Millstone, Reproducibility in Nanocrystal Synthesis? Watch Out for Impurities!, *ACS Nano*, 2020, **14**(6), 6359–6361.

32 Z. Khan, F. Javed, Z. Shamair, A. Hafeez, T. Fazal, A. Aslam, W. B. Zimmerman and F. Rehman, Current developments in esterification reaction: A review on process and parameters, *J. Ind. Eng. Chem.*, 2021, **103**, 80–101.

33 A. Singhal, S. N. Achary, J. Manjanna, S. Chatterjee, P. Ayyub and A. K. Tyagi, Chemical Synthesis and Structural and Magnetic Properties of Dispersible Cobalt- and Nickel-Doped ZnO Nanocrystals, *J. Phys. Chem. C*, 2010, **114**(8), 3422–3430.

34 D. Ito, S. Yokoyama, T. Zaikova, K. Masuko and J. E. Hutchison, Synthesis of Ligand-Stabilized Metal Oxide Nanocrystals and Epitaxial Core/Shell Nanocrystals *via* a Lower-Temperature Esterification Process, *ACS Nano*, 2014, **8**(1), 64–75.

35 E. C. Vreeland, J. Watt, G. B. Schober, B. G. Hance, M. J. Austin, A. D. Price, B. D. Fellows, T. C. Monson, N. S. Hudak, L. Maldonado-Camargo, A. C. Bohorquez, C. Rinaldi and D. L. Huber, Enhanced Nanoparticle Size Control by Extending LaMer's Mechanism, *Chem. Mater.*, 2015, **27**(17), 6059–6066.

36 A. W. Jansons and J. E. Hutchison, Continuous Growth of Metal Oxide Nanocrystals: Enhanced Control of Nanocrystal Size and Radial Dopant Distribution, *ACS Nano*, 2016, **10**(7), 6942–6951.

37 A. W. Jansons, K. M. Koskela, B. M. Crockett and J. E. Hutchison, Transition Metal-Doped Metal Oxide Nanocrystals: Efficient Substitutional Doping through a Continuous Growth Process, *Chem. Mater.*, 2017, **29**(19), 8167–8176.

38 S. R. Cooper, R. O. Candler, A. G. Cosby, D. W. Johnson, K. MØ. Jensen and J. E. Hutchison, Evolution of Atomic-Level Structure in Sub-10 Nanometer Iron Oxide Nanocrystals: Influence on Cation Occupancy and Growth Rates, *ACS Nano*, 2020, **14**(5), 5480–5490.

39 S. R. Cooper, L. K. Plummer, A. G. Cosby, P. Lenox, A. Jander, P. Dhagat and J. E. Hutchison, Insights into the Magnetic Properties of Sub-10 nm Iron Oxide Nanocrystals through the Use of a Continuous Growth Synthesis, *Chem. Mater.*, 2018, **30**(17), 6053–6062.

40 L. K. Plummer, B. M. Crockett, M. L. Pennel, A. W. Jansons, K. M. Koskela and J. E. Hutchison, Influence of Monomer Flux and Temperature on Morphology of Indium Oxide Nanocrystals during a Continuous Growth Synthesis, *Chem. Mater.*, 2019, **31**(18), 7638–7649.

41 L. K. Plummer and J. E. Hutchison, Understanding the Effects of Iron Precursor Ligation and Oxidation State Leads to Improved Synthetic Control for Spinel Iron Oxide Nanocrystals, *Inorg. Chem.*, 2020, **59**(20), 15074–15087.

42 K. Kim, J. Yu, J. Noh, L. C. Reimnitz, M. Chang, D. R. Gamelin, B. A. Korgel, G. S. Hwang and D. J. Milliron, Synthetic Control of Intrinsic Defect Formation in Metal Oxide Nanocrystals Using Dissociated Spectator Metal Salts, *J. Am. Chem. Soc.*, 2022, **144**(50), 22941–22949.

43 K. Kim, L. C. Reimnitz, S. Hum Cho, J. Noh, Z. Dong, S. L. Gibbs, B. A. Korgel and D. J. Milliron, Effect of Nonincorporative Cations on the Size and Shape of Indium Oxide Nanocrystals, *Chem. Mater.*, 2020, **32**(21), 9347–9354.

44 T. A. Knecht and J. E. Hutchison, Precursor and Surface Reactivities Influence the Early Growth of Indium Oxide Nanocrystals in a Reagent-Driven, Continuous Addition Synthesis, *Chem. Mater.*, 2023, **35**(8), 3151–3161.

45 A. W. Jansons, L. K. Plummer and J. E. Hutchison, Living Nanocrystals., *Chem. Mater.*, 2017, **29**(13), 5415–5425.

46 L. M. Bronstein, X. Huang, J. Retrum, A. Schmucker, M. Pink, B. D. Stein and B. Dragnea, Influence of Iron Oleate Complex Structure on Iron Oxide Nanoparticle Formation, *Chem. Mater.*, 2007, **19**(15), 3624–3632.

47 G. Cotin, C. Kiefer, F. Perton, D. Ihiawakrim, C. Blanco-Andujar, S. Moldovan, C. Lefevre, O. Ersen, B. Pichon, D. Mertz and S. Bégin-Colin, Unravelling the Thermal Decomposition Parameters for The Synthesis of Anisotropic Iron Oxide Nanoparticles, *Nanomaterials*, 2018, **8**(11), 881.

48 K. Nader, I. Castellanos-Rubio, I. Orue, D. Iglesias-Rojas, A. Barón, I. Gil de Muro, L. Lezama and M. Insausti, Getting insight into how iron(III) oleate precursors affect

the features of magnetite nanoparticles, *J. Solid State Chem.*, 2022, **316**, 123619.
49 S.-J. Park, S. Kim, S. Lee, Z. G. Khim, K. Char and T. Hyeon, Synthesis and Magnetic Studies of Uniform Iron Nanorods and Nanospheres, *J. Am. Chem. Soc.*, 2000, **122**(35), 8581–8582.
50 S. Sun, C. B. Murray, D. Weller, L. Folks and A. Moser, Monodisperse FePt Nanoparticles and Ferromagnetic FePt Nanocrystal Superlattices, *Science*, 2000, **287**(5460), 1989–1992.
51 S. Sun, H. Zeng, D. B. Robinson, S. Raoux, P. M. Rice, S. X. Wang and G. Li, Monodisperse MFe2O4 (M = Fe, Co, Mn) Nanoparticles, *J. Am. Chem. Soc.*, 2004, **126**(1), 273–279.
52 S. Sun and H. Zeng, Size-Controlled Synthesis of Magnetite Nanoparticles, *J. Am. Chem. Soc.*, 2002, **124**(28), 8204–8205.
53 T. Hyeon, S. S. Lee, J. Park, Y. Chung and H. B. Na, Synthesis of Highly Crystalline and Monodisperse Maghemite Nanocrystallites without a Size-Selection Process, *J. Am. Chem. Soc.*, 2001, **123**(51), 12798–12801.
54 M. D. C. Claramonte, F. G. Vilchez and A. P. Vialard, Thermal behaviour and heat capacity of some high molecular weight alcohols and esters used in pharmaceutical preparations, *Thermochim. Acta*, 1993, **222**(2), 209–218.
55 R. Hufschmid, H. Arami, R. M. Ferguson, M. Gonzales, E. Teeman, L. N. Brush, N. D. Browning and K. M. Krishnan, Synthesis of phase-pure and monodisperse iron oxide nanoparticles by thermal decomposition, *Nanoscale*, 2015, **7**(25), 11142–11154.
56 J. Llacer–Wintle, L. Hertle, S. Ziegler, E. Pellicer, A. G. Roca, J. Nogués, J. Puigmartí–Luis, B. J. Nelson, X. Z. Chen and S. Pané, A Simple In Situ Marker Guiding Shape–Controlled Synthesis of Iron Oxide Nanoparticles, *Adv. Funct. Mater.*, 2024, **34**(41), 2404113.
57 T. Hyeon, Chemical synthesis of magnetic nanoparticles, *Chem. Commun.*, 2003, (8), 927–934.
58 B. P. Pichon, O. Gerber, C. Lefevre, I. Florea, S. Fleutot, W. Baaziz, M. Pauly, M. Ohlmann, C. Ulhaq, O. Ersen, V. Pierron-Bohnes, P. Panissod, M. Drillon and S. Begin-Colin, Microstructural and Magnetic Investigations of Wüstite-Spinel Core-Shell Cubic-Shaped Nanoparticles, *Chem. Mater.*, 2011, **23**(11), 2886–2900.
59 M. F. Casula, Y.-w. Jun, D. J. Zaziski, E. M. Chan, A. Corrias and A. P. Alivisatos, The Concept of Delayed Nucleation in Nanocrystal Growth Demonstrated for the Case of Iron Oxide Nanodisks, *J. Am. Chem. Soc.*, 2006, **128**(5), 1675–1682.
60 R. Chalasani and S. Vasudevan, Form, Content, and Magnetism in Iron Oxide Nanocrystals, *J. Phys. Chem. C*, 2011, **115**(37), 18088–18093.
61 J. M. Orozco-Henao, F. L. Alí, J. C. Azcárate, L. D. Robledo Candia, G. Pasquevich, P. Mendoza Zélis, B. Haas, K. Coogan, H. Kirmse, C. T. Koch, C. Vericat, G. C. Lavorato and M. H. Fonticelli, Oxidation Kinetics of Magnetite Nanoparticles: Blocking Effect of Surface Ligands and Implications for the Design of Magnetic Nanoheaters, *Chem. Mater.*, 2024, **36**(22), 11095–11108.
62 E. D. Imhoff, A. Melnyk and C. M. Rinaldi-Ramos, Characterization and evaluation of commercial tracers for x-space magnetic particle imaging, *J. Magn. Magn. Mater.*, 2025, **620**, 172889.
63 C. Barrera, A. P. Herrera and C. Rinaldi, Colloidal dispersions of monodisperse magnetite nanoparticles modified with poly(ethylene glycol), *J. Colloid Interface Sci.*, 2009, **329**(1), 107–113.
64 C. Barrera, A. P. Herrera, N. Bezares, E. Fachini, R. Olayo-Valles, J. P. Hinestroza and C. Rinaldi, Effect of poly(ethylene oxide)-silane graft molecular weight on the colloidal properties of iron oxide nanoparticles for biomedical applications, *J. Colloid Interface Sci.*, 2012, **377**(1), 40–50.
65 A. Chiu-Lam, E. Staples, C. J. Pepine and C. Rinaldi, Perfusion, cryopreservation, and nanowarming of whole hearts using colloidally stable magnetic cryopreservation agent solutions, *Sci. Adv.*, 2021, **7**(2), eabe3005.
66 R. De Palma, S. Peeters, M. J. Van Bael, H. Van den Rul, K. Bonroy, W. Laureyn, J. Mullens, G. Borghs and G. Maes, Silane Ligand Exchange to Make Hydrophobic Superparamagnetic Nanoparticles Water-Dispersible, *Chem. Mater.*, 2007, **19**(7), 1821–1831.
67 R. Chantrell, J. Popplewell and S. Charles, Measurements of particle size distribution parameters in ferrofluids, *IEEE Trans. Magn.*, 1978, **14**(5), 975–977.
68 K. Lu, P. Goodwill, B. Zheng and S. Conolly, Multi-Channel Acquisition for Isotropic Resolution in Magnetic Particle Imaging, *IEEE Trans. Med. Imaging*, 2018, **37**(9), 1989–1998.
69 K. Lu, P. Goodwill, B. Zheng and S. Conolly, In *Reshaping the 2D MPI PSF to be isotropic and sharp using vector acquisition and equalization*, 2015 5th International Workshop on Magnetic Particle Imaging (IWMPI), 2015-03-01, IEEE, 2015, pp. 1–1.